

# Static and Dynamic Post-annealing Strategies for Roll-to-Roll Fabrication of DC Magnetron Sputtered Bismuth Telluride Thin Films onto Polymer Webs

*Xudong Tao<sup>a</sup>, Bryan W. Stuart<sup>a</sup>, Kening Wan<sup>b</sup>, James W. Murray<sup>c</sup>, Emiliano Bilotti<sup>b</sup>, Hazel E. Assender<sup>a\*</sup>.*

a: Department of Materials, University of Oxford, Parks Road, OX1 3PH.

b: School of Engineering and Materials Science, Queen Mary University of London, Mile End Road, E1 4NS.

c: Advanced Component Engineering Laboratory (ACEL), Faculty of Engineering, University of Nottingham, NG7 2RD.

Corresponding Author: Hazel E. Assender, [hazel.assender@materials.ox.ac.uk](mailto:hazel.assender@materials.ox.ac.uk)

**Keywords:** Roll-to-roll, Post annealing, Flexible/wearable thermoelectrics, Room-temperature sputtering, Bismuth Telluride

## **Abstract**

High-throughput roll-to-roll processes are desirable to scale up the manufacture of flexible thermoelectric generators. Whilst vacuum deposition onto a heated dynamic substrate presents a considerable engineering challenge, viable post-deposition in-line annealing processes are considered as an alternative to improve the functional performance of as-

deposited films. The effect of infrared and electron-beam irradiations of 1- $\mu\text{m}$  thick bismuth telluride thin films, produced by a vacuum roll-to-roll process for use as thermoelectric materials, were examined. Static vacuum oven and pulsed high-energy electron beam were also studied as control groups. All annealing strategies increased the crystallite size, and decreased the Te content. Only the static vacuum oven treatment was shown to significantly improve the film's crystallinity. After 1-hour annealing, the power factor improved by 400% (from 2.8 to  $14 \times 10^{-4} \text{ W/mK}^2$ ), which, to the knowledge of the authors, is the highest reported thermoelectric performance of post-annealed or hot-deposited Bi-Te films. As for in-line annealing, infrared and electron-beam post treatments improved the power factor by 146% (from 2.8 to  $6.9 \times 10^{-4} \text{ W/mK}^2$ ) and 64% (from 2.8 to  $4.6 \times 10^{-4} \text{ W/mK}^2$ ), respectively.

## 1. Introduction

Roll-to-roll (R2R) manufacture has attracted much attention as a low-cost means to fabricate flexible electronics. Device manufacture requires the deposition of in-line patterns of thin film materials. Wearable/flexible thermoelectric generators (TEGs) are of interest for portable electronics as a renewable (1), locally generated power source to minimise charging and energy storage requirements (2). As one of the best thermoelectric (TE) materials for operation at room temperature (RT), bismuth telluride ( $\text{Bi}_2\text{Te}_3$ ) has been extensively studied. It has been fabricated by various laboratory techniques, such as pulsed laser deposition (3), molecular beam epitaxy (4), chemical vapour deposition (5, 6), electro-deposition (7), (co-)evaporation (8-10), and (co-)sputtering deposition (11, 12). Sputtering and evaporation techniques show the most promising potential for scale-up to fabricate flexible electronics due to their dominance in industry, e.g. they are easily incorporated into R2R manufacturing (13) and are compatible with fabrication lines (14, 15), however, evaporation can lead to non-uniform coating. Evaporation of  $\text{Bi}_2\text{Te}_3$ , in particular, requires two co-evaporation boats and

power systems because of the different melting points and vapor pressures of Bi and Te, which again adds to the complexity for accurate process control. Hence, sputtering is employed in this study.

In laboratory scale studies, the focus has been on high-temperature deposition techniques because a columnar growth of  $\text{Bi}_2\text{Te}_3$  films can be achieved, significantly increasing the figure of merit,  $ZT$ , e.g. by  $\sim 50\%$  (16-18) ( $ZT = S^2T/\rho\kappa$ , where  $S$ ,  $T$ ,  $\rho$ , and  $\kappa$  are the Seebeck coefficient, the absolute temperature, the electrical resistivity and the thermal conductivity, respectively (19)). However, for high-throughput R2R processing, increasing the substrate temperature is a substantial challenge for flexible TEGs based on a deformable polymer substrate. Hence, for R2R processing at RT, a post annealing treatment is of interest because it can have a positive effect on the structural, electrical and thermoelectric properties of  $\text{Bi}_2\text{Te}_3$  films (12, 20, 21).

As well as morphology, stoichiometry can affect TE performance. As is common with vapour deposition from a mixed material source, the composition of the deposited Bi-Te may not match that of the sputtering target. Also, as one of the most common material treatment methods in semiconductor processing, annealing can adjust the stoichiometry of the deposited Bi-Te films by re-evaporation of Te under various annealing temperatures (20), because of its higher vapour pressure  $P$  ( $P_{\text{Bi}} = 10 \text{ Pa}$  at  $1041 \text{ K} \lll P_{\text{Te}} = 10 \text{ kPa}$  at  $1042 \text{ K}$ ). The electronic properties of the Bi-Te will depend on stoichiometry. For example, Te-rich Bi-Te is n-type semiconductor because of  $\text{Te}_{\text{Bi}}$  antisite defects generated by incorporation of excess Te atoms into Bi sites, while Bi-rich bismuth telluride is p-type due to  $\text{Bi}_{\text{Te}}$  antisite defects (22, 23). Hence, there may be a shift from n-type to p-type when annealing a Te-rich Bi-Te thin film. Both p-type (24, 25) and n-type (22, 23, 26) Bi-Te films with Bi-rich (46 – 66 at.% Bi) however have been observed following annealing, because of dislocations and oxygen

inclusions which act as donors contained in a thin film as a result of the materials processing. Hence, the nature of processing as well as the resulting stoichiometry is found to have a significant effect on properties. Thus, we have undertaken a study of films RT deposited onto a moving polymer substrate by DC magnetron sputtering, followed by a range of post-deposition annealing processes, to understand the impact upon materials TE properties.

To anneal Bi-Te films, a vacuum oven (23, 27, 28) is the most common and simple method. However, it is not a favourable approach for in-line R2R processing, for example annealing a wound roll of material will lead to the danger of the roll ‘blocking’ and being difficult to unwind. In recent years, more novel techniques have been proposed to enhance TE properties of Bi<sub>2</sub>Te<sub>3</sub> films such as Ebeam irradiation treatment (29, 30), which is a R2R compatible method, and could improve the film’s crystallisation by raising the temperature within the coating over a suitable depth (Ebeam irradiation depth:  $\sim 50\ \mu\text{m}$  (31)). As a comparison, in addition to Ebeam treatment, we also use infrared (IR) as another R2R compatible annealing technique. As the IR absorption regions of Bi-Te films (32, 33) and polymer substrates (34, 35) differ, it is possible to raise the coating temperature with the radiation whilst maintaining a minimally affected bulk polymer substrate. If either Ebeam and/or IR treatment methods are demonstrated to improve the coating properties, we could eliminate the challenges associated with post-rolling annealing whilst improving process efficacy for industrial manufacturing of flexible TEGs. Therefore, in this paper we explore the feasibility of various R2R compatible annealing strategies, particularly IR and Ebeam irradiations, for RT sputtered Bi-Te films on polymer substrates (i.e. polyimide (PI) sheets with a glass transition temperature,  $T_g$ , of 360°C) and their effect on TE properties.

## 2. Experimental details

### 2.1 Thin-film fabrication

A three-inch planar Bi<sub>2</sub>Te<sub>3</sub> sputtering target (Mi-Net Technology Ltd.) with a purity of 99.999% was used to deposit Bi-Te films by DC magnetron sputtering onto flexible PI sheets (Dupont Kapton 500 HN, 125 microns) using an Edwards Vacuum Coater Auto 306 system under a vacuum of  $\sim 8 \times 10^{-5}$  mbar ( $\sim 2 \times 10^{-5}$  mbar base pressure, 20 sccm Ar flow rate, and 0.1 kW power under 474 V voltage and 0.35 A current). The substrates were attached to a rotating drum at an in-line speed of 11.3 m min<sup>-1</sup>, and the drum-to-target distance was maintained as 6 cm. The film thickness was controlled at 1003 ( $\pm 5$ ) nm by adjusting the deposition time (i.e. the number of passes under the deposition source).

### 2.2 Post annealing

As-deposited films were annealed *via* four methodologies (see *Figure 1*), as summarised in *Table 1*. The first two approaches were static i) in a vacuum oven and ii) Ebeam irradiation as static standard references. The static vacuum oven was a custom-built high-vacuum furnace (capable of reaching  $\sim 1300$  °C at  $1 \times 10^{-5}$  mbar, with an approximate ramp rate of  $\sim 5.5$  °C min<sup>-1</sup>). Static annealing *via* Ebeam irradiation was carried out with a pulsed electron source using a Sodick PF32A Electron Beam Machining system in  $5 \times 10^{-4}$  mbar of Argon with an irradiation distance and accelerating voltage of 300 mm and (10 & 13 kV), respectively. This low-energy (<40 keV) high current (10 – 25 kA) pulsed electron beam irradiation could give a rapid and homogenous application of energy density 0.3-20 J/cm<sup>2</sup> over an area of  $\sim 60$  mm diameter with a pulse duration of 2 – 4  $\mu$ s, and penetration depth up to 10  $\mu$ m (36).

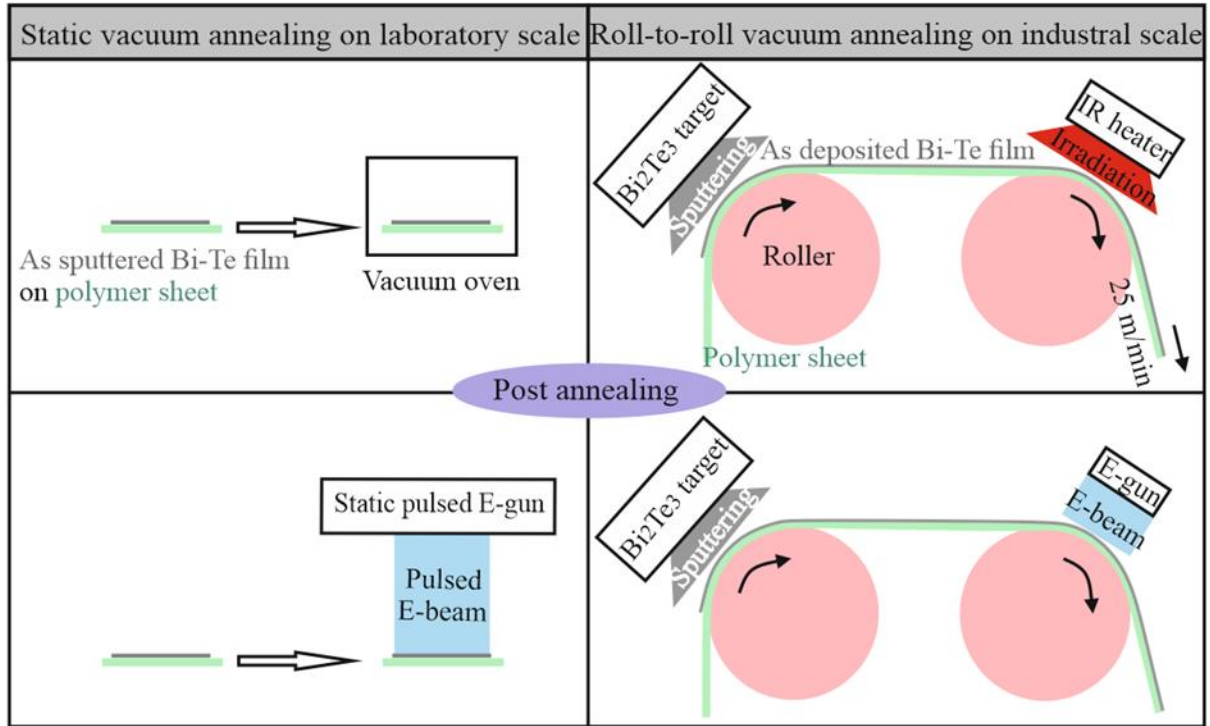


**Figure 1.** Schematics of four different post annealing strategies: static vacuum oven, static Ebeam irradiation, dynamic IR irradiation and dynamic Ebeam irradiation, under conditions of 250/350 °C ( $1 \times 10^{-5}$  mbar), 10/13 kV ( $5 \times 10^{-4}$  mbar), 250/350 °C ( $1.5 \times 10^{-4}$  mbar, 25 m  $\text{min}^{-1}$ ), and 5.8/7.3 kV ( $1.5 \times 10^{-4}$  mbar, 25 m  $\text{min}^{-1}$ ), respectively.

To further investigate the feasibility of annealing approaches in R2R processing, two dynamic strategies (IR and Ebeam irradiations) were trialed at  $1.5 \times 10^{-4}$  mbar (a typical vacuum level for a low-cost high throughput R2R process) with samples fixed to a rotating drum (25 m  $\text{min}^{-1}$ ) in an Aerre Machine Vacuum webcoater with Ebeam current: 100 mA (5.8 kV) and 170 mA (7.3 kV). The IR annealing (0.5 kW IR source: 1500 – 5600 nm, i.e. 0.2214 – 0.8266 eV, corresponding to  $\sim 20000 - 100000 \text{ cm}^{-1}$  of absorption coefficient on Bi-Te film (37, 38)) was initially conducted in the same condition but with the sample held statically under the IR source to determine the effect of maximum irradiation temperature. To measure the dynamic temperature on the film surface (i.e. the temperature variation as the

drum rotates), a temperature data logger (EL-USB-TC-LCD EasyLog) measured a Bi-Te coated thermocouple, attached to the rotating roller.

**Table 1.** Conditions of various annealing approaches.

Annealing means	Vacuum base pressure (mbar)	Anneal temp. /condition	Time to setting condition (min)	Anneal time (min)	Take-out temp. /time	Drum speed (m/min)
Comparison of different methods (section 3.1 & 3.2)						
Static vacuum oven	1×10 <sup>-5</sup>	250°C	~60	60	50°C	Static
		350°C				
Static pulsed Ebeam	5×10 <sup>-4</sup>	10 kV	-	60	-	
		13 kV				
Static IR	1.5×10 <sup>-4</sup>	250°C	~8	60	50°C	
		350°C				
Dynamic Ebeam	1.5×10 <sup>-4</sup>	5.8 kV	~3	60	5 mins	25
		7.3 kV				
Time-dependency (section 3.3)						
Dynamic IR	1.5×10 <sup>-4</sup>	145°C	~8	1 - 60	50°C	25
Dynamic Ebeam	1.5×10 <sup>-4</sup>	7.3 kV	~3	1 - 60	5 mins	25

\*Note that for the dynamic processes the samples are attached to a rotating drum of approx. 1.8 m circumference, rotating at  $25 \text{ m min}^{-1}$ , thus the sample, during the annealing process is not continuously underneath the annealing source, but passes underneath it multiple times.

## 2.3 Materials characterisation

Sample-to-sample variation has been included in uncertainty values for all quantitative characterisation presented. The run-to-run variation was determined in three independent batches, showing variations of 4.4% in thickness, 3.0% in electrical measurements and 1.5% in Seebeck results.

### Thickness measurement and structural characterisation

Thin film Bi-Te thickness was obtained using a Veeco DekTak 6 M stylus profiler at ten different locations, which measured the step height between the coating and substrate, applied

to partially masked silicon wafers. The film thickness was 1003 ( $\pm 5$ ) nm with a rotating deposition rate of  $\sim 0.6 \text{ nm s}^{-1}$ . (The change of film thickness after various anneals is less than 5 nm, which is negligible in this study).

The crystal-structural analysis of films deposited contemporaneously with those for other characterisation methods onto very thin PI film was performed by x-ray diffraction XRD (Rigaku Miniflex diffractometer) using Cu  $k\alpha$  radiation ( $\lambda = 0.154 \text{ nm}$ ) at 30 kV and 10 mA over a range of  $2\theta$  between  $10^\circ$  and  $80^\circ$  with a step size of  $0.007^\circ$ . The coated thin PI film was adhered to a glass substrate to keep it flat during measurement. The grain size and lattice strain were calculated from the broadening of XRD peaks using Williamson-Hall method (39) in X'pert Highscore Plus software, with a removal of instrumental broadening by assuming a Gaussian profile and using a polycrystalline Si bulk as a standard reference.

$$\beta \cos(\theta) = \frac{K\lambda}{D} + 4\eta \sin(\theta) \quad (1)$$

where  $\theta$  is the Bragg diffraction angle,  $\beta$  is the full width of the Bragg peak at half maximum (FWHM),  $\lambda$  is the radiation wavelength (0.154 nm),  $D$  is the crystallite size,  $\eta$  is the lattice strain and  $K$  is the Scherrer constant (0.62 – 2.08 dependent on the crystal structure (40)). With the plot of  $\beta \cos(\theta)$  and  $4\sin(\theta)$ , the slope of fitting line estimates the average lattice strain and the y-intercept estimates the average crystallite size.

The surface morphology of the thin films on PI was characterised using a field-emission scanning electron microscope (FE-SEM Zeiss Merlin), with  $50 \text{ k} \times$  magnification, 3 kV voltage, 100 pA probe, and 5 mm working distance. As the composition of the film may depend on the annealing conditions, elemental composition and mapping were obtained using Energy Dispersive X-Ray spectroscopy (EDX) within a (Zeiss Evo) SEM using point ID



mode over 12 independent points in 3 locations, and in mapping mode of a FE-SEM (50 k × magnification, 8.5 mm working distance and 3 kV voltage), respectively.

### **Thermoelectric characterisation**

The electrical resistivity ( $\rho$ ) was calculated using Equation (2) by the film thickness, and the sheet resistance obtained from an in-house custom four point probe system (at a mean of 4 different locations). Under an applied current of  $10^{-2} - 10^{-5}$  A through the outer two probes, the voltage was measured across the two inner probes *via* an Agilent 34420 A Nano Volt/Micro Ohm meter.

$$\rho = R_s \cdot t = \frac{\pi}{\ln 2} \left( \frac{V}{I} \right) \cdot t \quad (2)$$

where  $\rho$  is the electrical resistivity,  $R_s$  is the sheet resistance,  $t$  is the film thickness,  $V$  is the voltage and  $I$  is the current.

The Seebeck coefficient ( $S$ ) was measured using an MMR Tech. Seebeck effect system at 300 K under nitrogen atmosphere applying temperature differences from 0.1 to 0.45 K, determined by the ratio of an output voltage generated across the film surface to the temperature difference. An average result was obtained from at least eight measurements. The TE performance of films, power factor ( $PF$ ), was calculated (see Equation (3) combining effects of both  $\rho$  and  $S$ ).

$$PF = \frac{S^2}{\rho} \quad (3)$$

To analyse the thermoelectric performance, Hall measurement and UV-Vis spectroscopy were used to obtain the film's carrier concentration/mobility and band gap, respectively.

The carrier concentration and mobility of films were measured in an in-house made Hall effect measurement system, using a square-size specimen ( $1\text{ cm} \times 1\text{ cm}$ ) with an evaporated layer ( $110 \pm 5\text{ nm}$ ) of silver at the four corners ( $0.1\text{ cm} \times 0.1\text{ cm}$ ), magnets (0.165 T), and a Keysight 82901A as current source and voltammeter.

The band gap ( $E_g$ ) of film was obtained using Tauc plot from the absorbance spectra (200 – 3300 nm wavelength) using a Cary Varian 5000 UV-visible-NIR spectrometer.

### **Mechanical characterisation**

Tensile tests were performed in a Linkam Scientific TST350 testing stage using a 200 N load cell. Dogbone samples were prepared with the narrow section between grips of size  $26\text{ mm} \times 7\text{ mm}$ .

To analyse the effect of IR irradiation on mechanical properties of the coating on PI, FTIR spectra were recorded using a Varian Excalibur FTS 3500 FTIR Spectrometer with attenuated total reflection (ATR) in the mid IR range  $7000\text{ to }350\text{ cm}^{-1}$ , obtaining 16 scans for co-averaged results.

## **3. Results and discussion**

### **3.1 Structural properties of as deposited/annealed Bi-Te films**

The XRD patterns and elemental compositions of as-deposited and post-annealed Bi-Te films are shown in *Figure 2 a & b*. The average crystal size and strain were obtained from Williamson-Hall plots (see *Figure 2 c*), as summarised in *Table 2*. *Figure 3* shows the SEM micrographs of as-deposited and post-annealed Bi-Te films. The effect of post-deposition anneal is clearly revealed through these SEM images, although the impact varies for different annealing techniques.

### **As-deposited film**

The as-deposited film showed characteristic diffraction peaks at  $2\theta$  of  $27.7^\circ$ ,  $38.2^\circ$ ,  $57.1^\circ$  and  $62.7^\circ$ , corresponding to (0 1 5), (1 0 10), (2 0 10) and (1 1 15) planes, respectively, as expected in a standard  $\text{Bi}_2\text{Te}_3$  phase (ICSD #193330). XRD peaks (0 1 5) and (1 0 10) were observed for both hot and RT deposition of  $\text{Bi}_2\text{Te}_3$  film on polymer/rigid substrates (27, 29, 30, 41-50), due to their inherently strong reflection. Unlike with hot deposition on rigid substrates (30, 41, 51), orientational growth (beneficial to the electrical property of films) was not observed in our study, consistent with literature for RT deposition (43, 52).

The as-deposited film showed low/broad peaks indicative of small crystallites (27, 29), as well as a possibility of overlapping peaks (53) of different phases with a similar crystallographic structure to  $\text{Bi}_2\text{Te}_3$ , e.g.  $\text{BiTe}$  and  $\text{Te}$  (*Figure 2 a*). In addition, some of minor diffraction peaks (e.g.  $43.8^\circ$ ) were indexed as metallic  $\text{Te}$  (23). Therefore, other phases, including  $\text{Te}$ -rich phases (31) could coexist with  $\text{Bi}_2\text{Te}_3$  phase, forming structural defects between different phases (48). This could have a significant influence on TE behaviours.

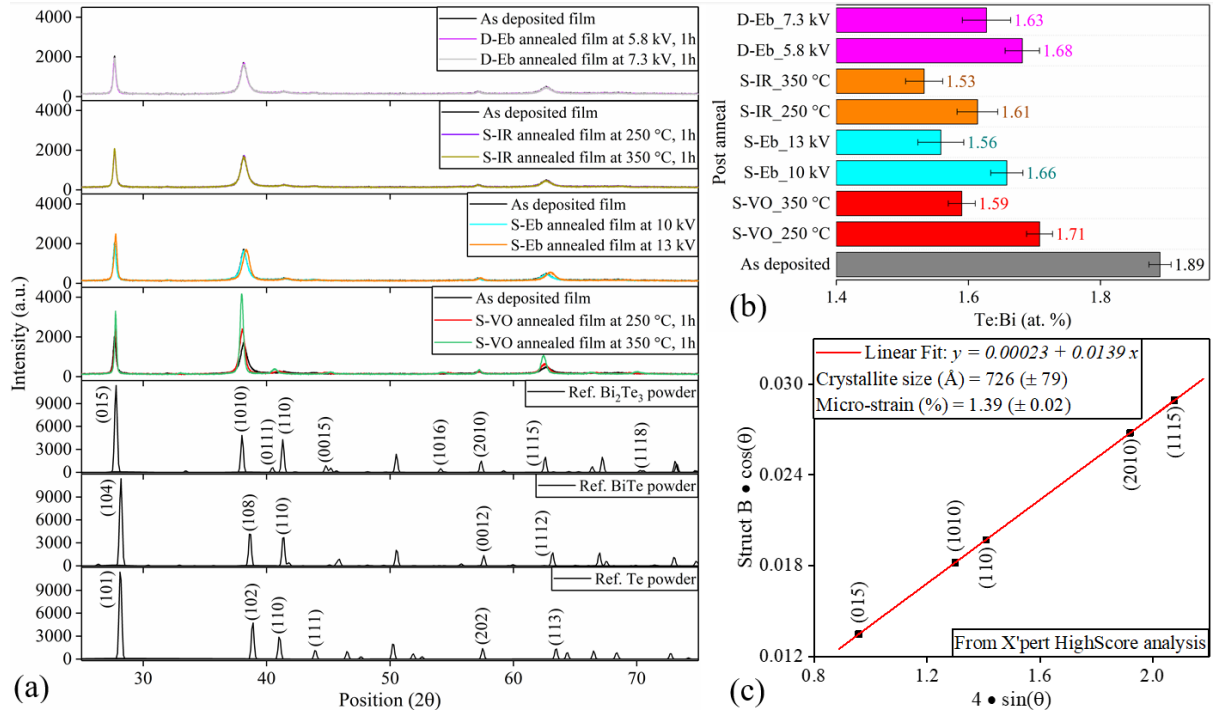


**Figure 2.** (a) XRD patterns of as-deposited and post-annealed Bi-Te films, with the reference traces: Te (ICSD #40042), BiTe (ICSD #30526), and Bi<sub>2</sub>Te<sub>3</sub> (ICSD #193330) powders; (b) Te/Bi ratio determined from EDX before and after various treatments; (c) Example Williamson-Hall analysis (as-deposited film), where Struct B = the observed FWHM – the instrumental broadening,  $\theta$  is the Bragg diffraction angle. (S-VO denotes static vacuum oven system in laboratory scale; S-Eb denotes static pulsed Ebeam system in laboratory scale; while S-IR and D-IR denote static and dynamic infrared radiation, respectively; D-Eb denotes dynamic Ebeam system in a R2R webcoater).

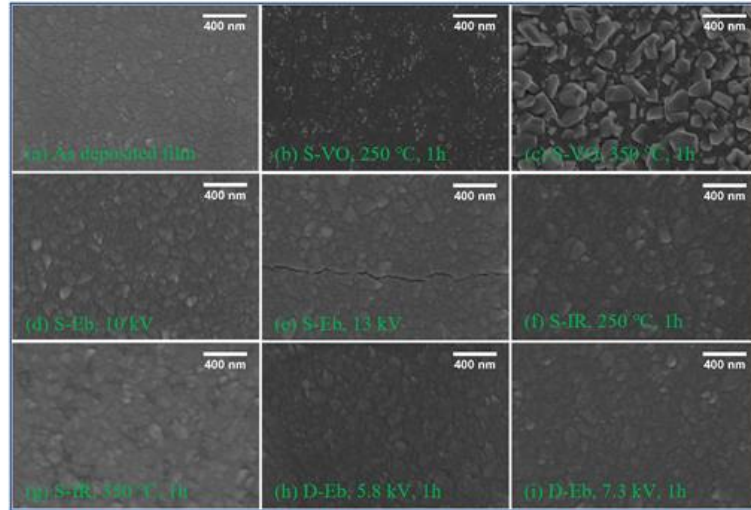
**Table 2.** The average crystallite size, micro-strain and lattice parameters of as-deposited and post-annealed films from Williamson-Hall plot in X'pert Highscore Plus software.

Specimens	Crystallite size [Å]	Micro-strain [%]	Lattice parameters [Å]	
			a = b (± 0.003)	c (± 0.03)
As-deposited	726 (± 79)	1.39 (± 0.02)	4.36	30.31
S-VO_250 °C	1333 (± 284)	1.06 (± 0.02)	4.43	30.35

<b>S-VO_350 °C</b>	1341 ( $\pm 252$ )	0.81 ( $\pm 0.01$ )	4.46	30.25
<b>S-Eb_10 kV</b>	1031 ( $\pm 153$ )	1.63 ( $\pm 0.01$ )	4.39	30.37
<b>S-Eb_13 kV</b>	848 ( $\pm 48$ )	1.75 ( $\pm 0.07$ )	4.37	30.20
<b>S-IR_250 °C</b>	740 ( $\pm 87$ )	1.39 ( $\pm 0.02$ )	4.36	30.31
<b>S-IR_350 °C</b>	742 ( $\pm 98$ )	1.39 ( $\pm 0.02$ )	4.35	30.35
<b>D-Eb_5.8 kV</b>	788 ( $\pm 87$ )	1.39 ( $\pm 0.01$ )	4.37	30.30
<b>D-Eb_7.3 kV</b>	814 ( $\pm 77$ )	1.44 ( $\pm 0.01$ )	4.37	30.32

From the EDX result (*Figure 2 b*), the as-deposited film was more Te-rich (1.9 at.%) than the Bi<sub>2</sub>Te<sub>3</sub> target (1.5 at.%) and, to a lesser extent, also after heat or radiation treatments, due to a preferential vaporisation of Te elements in the film during the annealing process (20, 23, 28). In this study, the Te-rich film was n-type, confirmed by both Seebeck and Hall results, consistently with literature (24, 25), remaining n-type even after heat or radiation treatments.

Part A:



Part B:

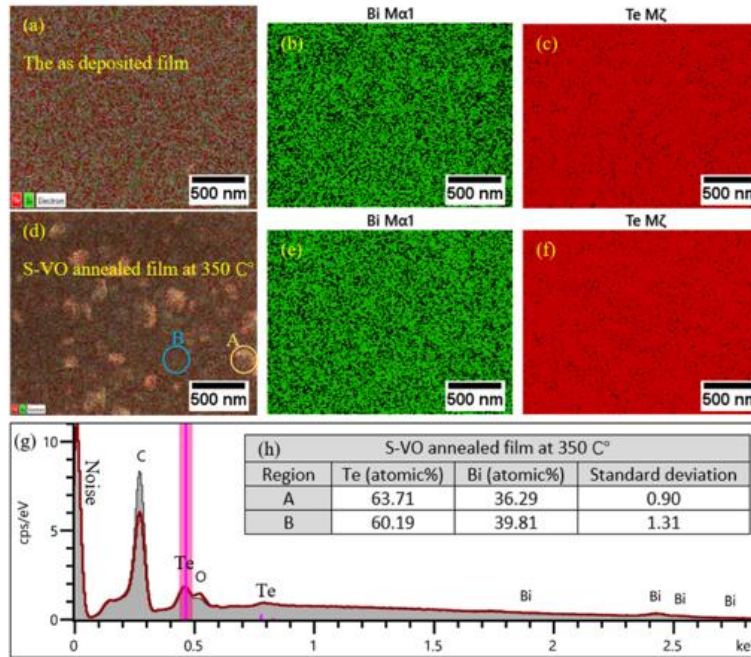


**Figure 3.** Part A: SEM images of the as-deposited and post-treated Bi-Te films: (a) the as-deposited film; (b-c) films annealed in a static vacuum oven at 250°C and 350°C; (d-e) films annealed in a static Ebeam system at 10 kV and 13 kV; (f-g) films annealed in static IR radiation at 250°C and 350°C; (h-i) films annealed in a dynamic Ebeam treatment at 5.8 kV and 7.3 kV. Part B: The elemental mapping of: (a-c) the as-deposited film and (d-f) the film annealed in vacuum oven at 350°C; (g) EDX spectra of the as-deposited film (the grey profile line) and the film annealed in vacuum oven at 350°C (the red profile line); (h) the

composition in regions 'A' and 'B' in (d) (an average of 6 different locations) of the film annealed in vacuum oven.

### **Static vacuum-oven annealed film**

Films annealed in a vacuum oven showed a significant enhancement in crystallinity, with more intense crystalline peaks. The peak of the as-deposited film at  $38.17^\circ$  (FWHM =  $0.358^\circ$ ) narrowed to  $0.248^\circ$  and shifted to  $37.99^\circ$ , approaching the expected position for reference  $\text{Bi}_2\text{Te}_3$ , for a  $350^\circ\text{C}$  anneal. The same phenomenon was observed for the  $62.7^\circ$  peak. These observations reflect an increase in crystal size to 134.1 nm and a decrease in lattice strain from 1.39% to 0.81% (Table 2), associated with the annealing. After annealing, the relative intensity of (0 1 5), (1 0 10) and (1 1 15) peaks changed and the (1 0 10) plane gradually showed the strongest intensity, indicating a change in the preferential orientation of crystallites (27, 54). In addition, the minor diffraction peak (1 1 0) at  $41.5^\circ$  (possibly corresponding to Te phase since the film was Te-rich) completely vanished while a new peak at  $40.6^\circ$  appeared to match the (0 1 11) plane in reference  $\text{Bi}_2\text{Te}_3$ , indicating a decrease in Te content with annealing (28) and more or differently orientated crystallites in the  $\text{Bi}_2\text{Te}_3$  phase.

From the SEM imaging (Figure 3 A b & c), after annealing in the vacuum oven, protruding large crystals appeared on the film surface and appeared to grow with the annealing temperature. This kind of phenomenon has already been observed and reported as Sb-rich/Te-rich crystalloid precipitates in annealing Bi-Sb-Te and Sb-Te films (46, 55, 56), but not yet observed for Te-rich precipitates in annealing Bi-Te films (23, 27, 28, 50). EDX maps (Figure 3 B d & h) indicated that the protruding grains were modestly Te-rich. Te-rich precipitates formed when annealing as the Te atoms became mobile and tended to migrate/precipitate at the grain boundaries and to the surface of annealing films.

### Static Ebeam annealed film

In terms of annealing using a static pulsed Ebeam system, there were some increases in grain size from the XRD pattern, greater for the sample annealed at 10 kV (*Table 2*). Both Ebeam-treated specimens showed an increased lattice strain, as observed in (30). Some reports of Ebeam treatment suggested little or no modification (29) of the crystallinity of Bi-Te, although one report of Bi-Sb-Te (31) noted a small increase in crystallite size with Ebeam treatment.

The 13 kV Ebeam irradiation was shown to damage the film (for example due to thermal expansion) as shown by cracks observed on the film surface (see *Figure 3 A e*), which dramatically affected the electrical properties (see part 3.2) giving a very high resistance.

### Dynamic Ebeam and static IR annealed films

Regarding both IR and Ebeam treatments in the webcoater, there was no substantial change in XRD peak positions. This modest increase in crystallite size perhaps seen from the XRD was also observed in the SEM (*Figure 3 A f-i*), though the grain growth is less obvious at the surface than for the vacuum oven-treated samples.

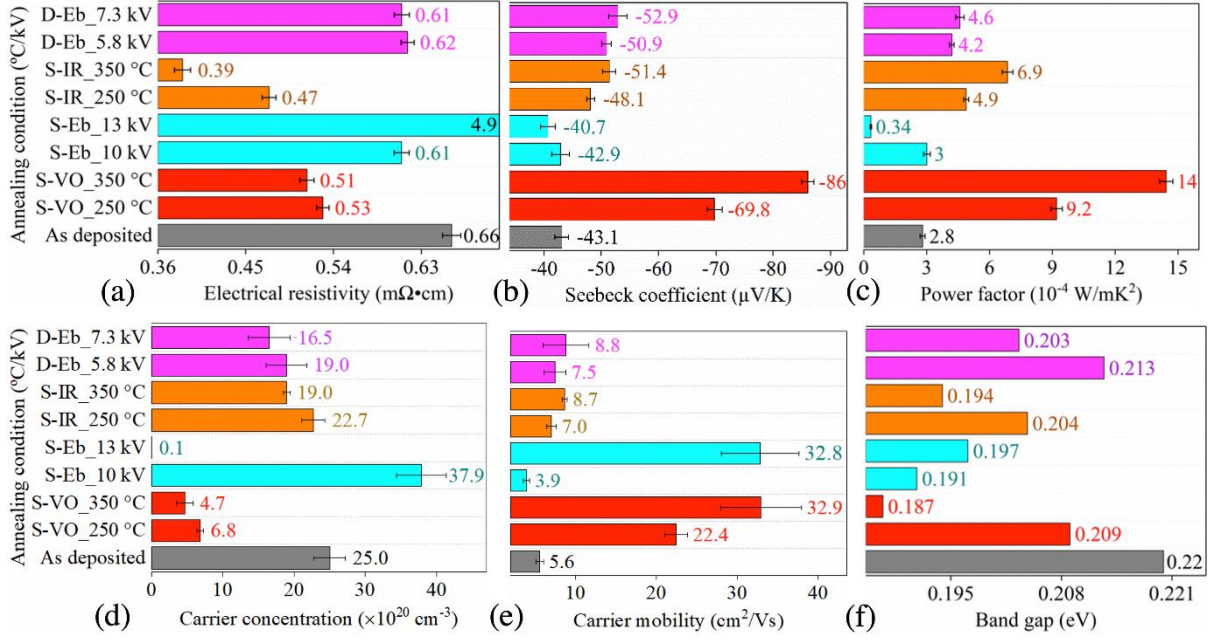
These observed changes in crystal size and stoichiometry will be discussed below, in the context of the TE characteristics of the material.

## 3.2 Thermoelectric behaviour of as-deposited and post-annealed Bi-Te films

*Figure 4 A* shows  $\rho$ ,  $S$  and  $PF$  of as-deposited and post-annealed Bi-Te films. To analyse the variation of  $\rho$  and  $S$ , we also plot the carrier concentration ( $n$ ), mobility ( $\mu$ ) and  $E_g$  of films. To achieve a high  $PF$ , a low  $\rho$  but a high  $S$  are required according to Equation (3). The data fit the expected relations  $\rho \propto \frac{1}{\mu \cdot n}$  (57),  $S \propto \frac{1}{n^{2/3}}$  (58) and  $S \propto \mu^{0.2}$  (59) well (except the damaged S-Eb 13 kV), as shown in *Figure 4 B (a-c)*.



### Part A:



### Part B:

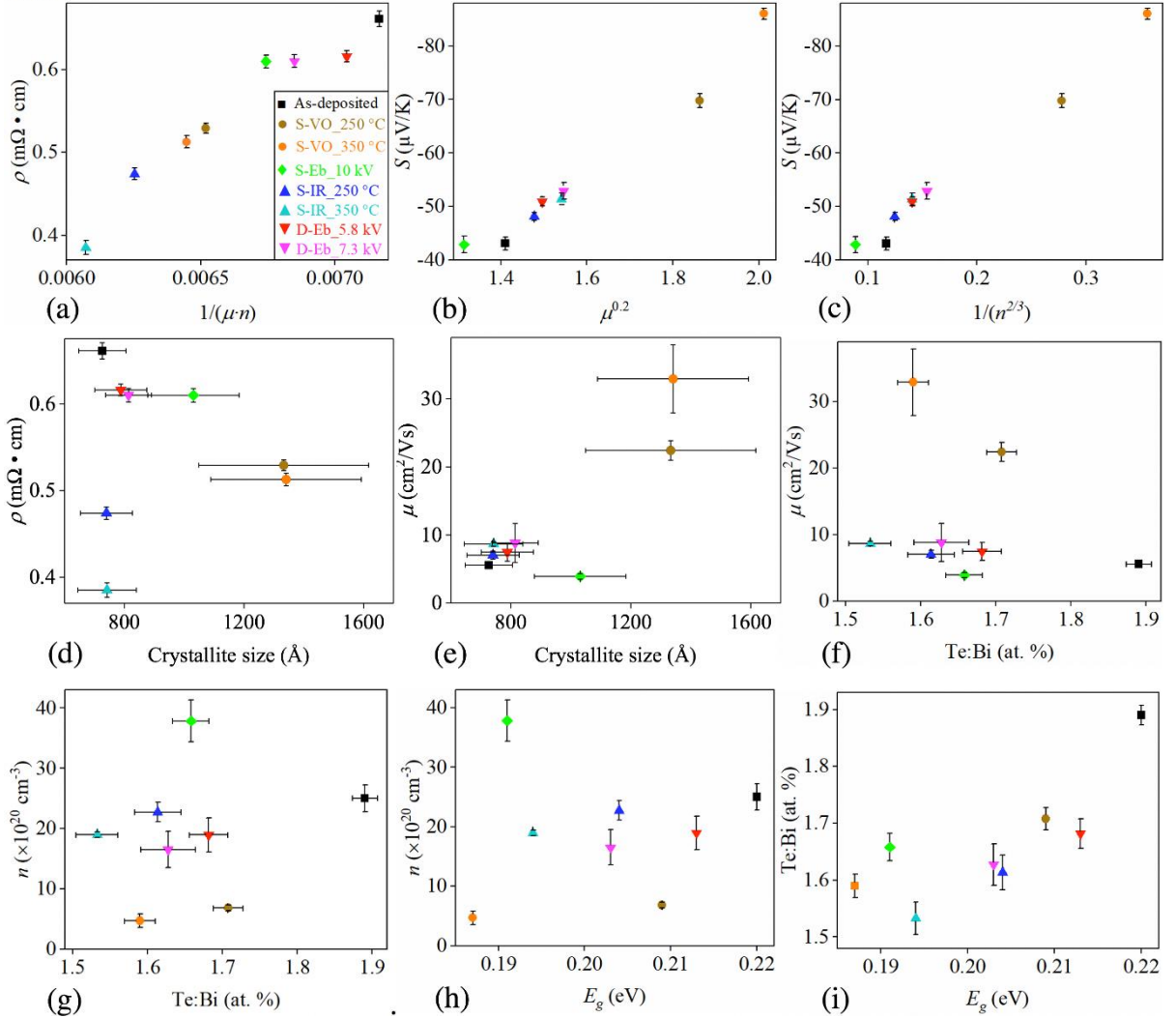


**Figure 4.** Part A: (a)  $\rho$ , (b)  $S$ , (c)  $PF$ , (d)  $n$ , (e)  $\mu$  and (f)  $E_g$  of as-deposited and post-annealed films; Part B: (a-c) the expected relations of  $S$  and  $\rho$  with  $n$  and  $\mu$ ; Plots of (d)  $\rho$  vs crystallite size, (e)  $\mu$  vs crystallite size, (f)  $\mu$  vs ratio of Te:Bi, (g)  $n$  vs ratio of Te:Bi and (h)  $n$  vs  $E_g$ ; and (i) ratio of Te:Bi vs  $E_g$ .

### Electrical resistivity and Seebeck coefficient

The as-deposited film exhibited the highest  $\rho$  (0.66 m $\Omega$ ·cm) and a relatively small  $S$  (43.1  $\mu$ V/K). The vacuum-oven annealing at 350°C decreased  $\rho$  to 0.51 m $\Omega$ ·cm while significantly increased  $S$  to 86  $\mu$ V/K. The static pulsed Ebeam annealing at 13 kV increased  $\rho$  tenfold due to cracks formed in the film, while the 10 kV Ebeam treatment kept  $\rho$  and  $S$  approximately unchanged. In terms of the IR annealing, a significant decrease in  $\rho$  (from 0.66 to 0.39 m $\Omega$ ·cm) was observed, accompanied with a slight increase in  $S$  (from 43.1 to 51.4  $\mu$ V/K). After Ebeam annealing in webcoater, there was no obvious change in  $\rho$  but an increase in  $S$  was observed from 43.1 to 52.9  $\mu$ V/K.

The variation in both  $\rho$  and  $S$  is a complicated competitive relation between  $n$  and  $\mu$ . We can consider the following factors that could affect both  $n$  and  $\mu$ .

- (1) The change in grain size on boundary scattering mechanism (50);
- (2) The improvement of crystallinity on scattering mechanism (30, 60);
- (3) The change in film composition (61, 62);
- (4) The content variation of defects as donors (50);
- (5) The variation in band gap with annealing process (63);
- (6) The modification of the energy barrier at a grain boundary (64).

Results related to these effects are plotted in *Figure 4 B (d-i)*.

(1 - 3) These three effects have significant impacts on  $\mu$ . *Figure 4 B (e)* shows that  $\mu$  broadly increases as crystallite size increases because of a reduced crystallite boundary carrier scattering. There does not appear to be a strong correlation between mobility and composition (*Figure 4 B (f)*). A low  $\mu$  for S-Eb could be due to the observed sample damage by the E-beam treatment.

(4 - 6) These effects significantly influence  $n$ . Post annealing treatments do tend to lead to a lower Te content, as expected from the greater volatility of Te. With  $\text{Te}_{\text{Bi}}$  defects removed,  $n$  would expect to decrease with lower Te content, because  $\text{Te}_{\text{Bi}}$  antisite defects (i.e. the substitution of Te atoms into Bi vacancies) act as the major source of electron donors (4) in Te-excess Bi-Te films. The variation of  $n$  with Te:Bi ratio, shown in *Figure 4 B (g)*, does not show a strong trend as expected from this defect model. It may be that the very high Te content of these films reflects the formation of regions of the material that are predominantly Te (for which there are indications in the XRD data), which themselves would not act as defects in the Bi-Te material. The  $E_g$  of the material is shown to increase with increasing Te:Bi (*Figure 4 B i*), i.e. it is lower for the annealed materials. This may be due to doping effects introducing carrier levels in the  $E_g$ , or from changes in ordering/confinement length in the material. One might expect  $n$  to increase with decreasing  $E_g$  because of the dual effect of the increased number of intrinsic carriers with a lower  $E_g$ , and any extrinsic carriers formed by increased dopant levels that would have the effect of decreasing the observed  $E_g$ . However, we observe (*Figure 4 B h*), if anything, a slight decrease in  $n$  with decreasing  $E_g$ , suggesting that (1) any decrease in  $E_g$  does not lead to useful charge carriers e.g. due to the formation of trapped charge levels, or (2) the observed decrease in  $E_g$  may originate from material that does not contribute significantly to the charge conduction as measured by the Hall effect e.g. in highly disordered or non-stoichiometric material. Indeed, there is little or no correlation observed between  $n$  and the average stoichiometry of the film (Te:Bi), as

observed in *Figure 4 B g*). In addition to the consideration of extrinsic (due to doping) and intrinsic (due to a reduction in  $E_g$ ) carriers, we should also consider the energy barrier to carrier transport at grain boundaries (6), which will act to decrease the effective  $n$ . Room-temperature sputtered Bi-Te film is Te-rich and poorly crystalline, and most likely, the excess/amorphous Te phases exists at the grain boundaries, acting as an energy barrier to filter the carriers moving in plane. If Te precipitates form at grain boundaries on annealing (*Figure 3 A c*), this could increase the energy barrier leading to a significant decrease in  $n$  (*Figure 4 A d*).

This analysis of trends in  $\mu$  and  $n$  demonstrates that a number of factors come together to give rise to the observed changes in TE performance, and that these can be related to the observed changes in microstructure and composition of the films as a result of annealing. It also serves to demonstrate how not only the deposition processes, but also any subsequent treatments are factors in the TE performance of the material.

### **Power factor**

$PF$  is a measure of TE performance based on  $\rho$  and  $S$  (see Equation (3)). All annealing approaches tried here showed an enhancement in  $PF$ . The film annealed in the vacuum oven at 350°C exhibited the highest  $PF$  ( $14 \times 10^{-4}$  W/mK<sup>2</sup>), ~5-times higher (400%) than that of the as-deposited film. Such a  $PF$  is also higher than the latest reported values of post-annealed/hot-deposited Bi-Te films fabricated by sputtering ( $11.45 \times 10^{-4}$  W/mK<sup>2</sup>, 2017, (28)). However, a vacuum oven is not a feasible method for R2R processing. Considering annealing approaches compatible with a R2R processes, a dynamic Ebeam treatment (7.3 kV) showed an increase in  $PF$  by 64% compared to the as-deposited film while a static IR irradiation (350°C) increases  $PF$  by 146%. According to the irradiation/penetration depth of Ebeam (~ 50  $\mu$ m (31)) and IR (~400 - 700 nm (65)) on Bi-Te films, the Ebeam treatment can

directly anneal the whole thickness of the coating, while the IR treatment is only expected to directly treat the top region, thus the underlying material will only be annealed by any conduction of heat from the top. If this is the case, then it opens up the possibility that IR annealing would be able to significantly improve the TE behavior of thinner layers that may be more appropriate for R2R-deposited material (66). A study of the effects of film thickness on the effectiveness of the post-deposition annealing is beyond the scope of this report, but would be an important consideration for further work on optimizing a preferred annealing method.

Although both Ebeam and IR techniques each could improve the TE property of the as-deposited Bi-Te film, IR irradiation performed better. However, these results were obtained from a 60-min anneal which was a long time for a fast R2R process (requiring 833 rotational passes in this case), and the IR irradiation was performed in a static condition rather than a dynamic condition. The effectiveness of an anneal will decrease as the annealing time decreases (67, 68). To achieve a real R2R post-annealing process, investigating the extent of the effect of treatment time in R2R processing is necessary.

### **3.3 Decreasing the treatment time for R2R annealing approaches**

When comparing static IR annealing to that from multiple passes of a moving substrate, the temperatures achieved at the substrate need to be considered. In *Figure 5 a*, it is clearly observed that a half-power IR heater (250 W) could reach 350°C in a static condition and decreased to 57°C when the drum rotated at 25 m min<sup>-1</sup>. To achieve the highest temperature during drum rotation, a full power (500 W) was applied to the IR source. In *Figure 5 b*, the approximate temperature varied between ~150°C and ~138°C as the drum rotated.

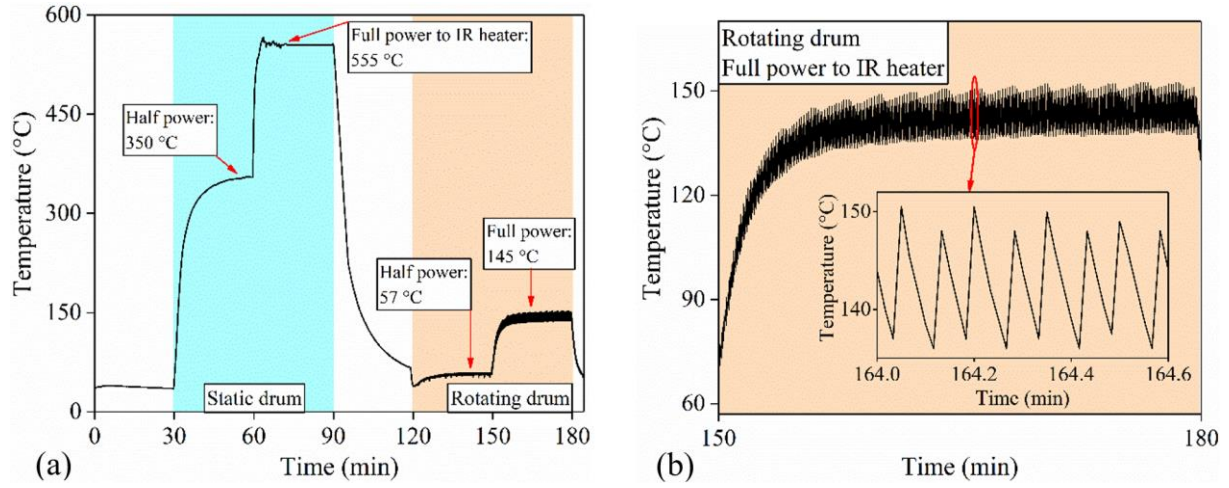


**Figure 5.** (a) The variation of temperature on the drum in static and dynamic situations under half/full powers of an IR source, and (b) The temperature on a rotating drum under full power to the IR heater (the temperature reached the highest when facing the IR heater but reached the lowest when rotated away from the heater).

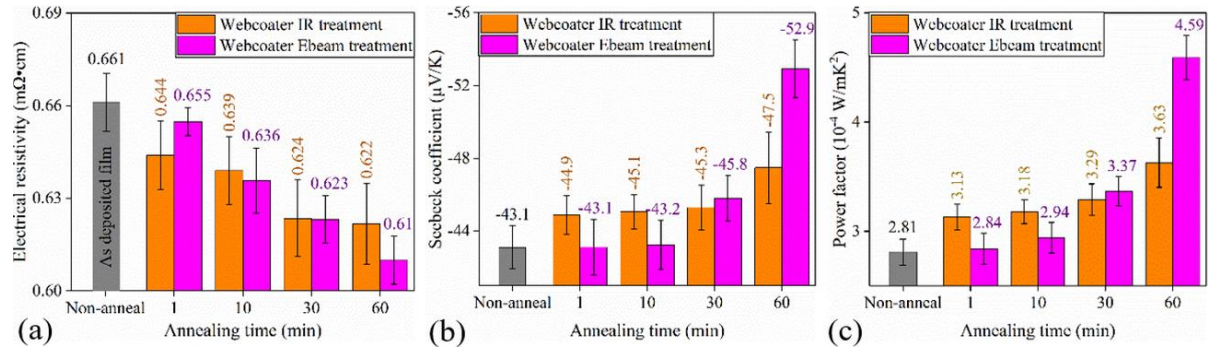


**Figure 6.** Plots of (a)  $\rho$ , (b)  $S$  and (c)  $PF$  for Bi-Te films with various annealing times of dynamic IR and Ebeam irradiations in webcoater (moving drum:  $25 \text{ m min}^{-1}$ ).

The variations of  $\rho$ ,  $S$  and  $PF$  as a function of annealing time have been obtained, as shown in Figure 6. Both dynamic Ebeam and IR treatments were performed on as-deposited films on a rotating drum ( $25 \text{ m min}^{-1}$ ), under 7.3 kV and 145 °C, respectively. Both approaches showed an improvement in electrical conductivity and Seebeck coefficient with annealing time. Similar to previous reports (67, 68), a shorter anneal time had less effect, indicating that a long time (especially for the dynamic anneal,  $>1 \text{ h}$ ) is required to maximise the TE

performance under this annealing condition, but after a very long annealing time we might expect that further improvements in the TE performance would reduce and eventually stop. In this study, we do not carry on further analysis on very long annealing time as this is incompatible with the R2R process.

The dynamic IR annealing is less effective to enhance  $PF$  compared with the static IR annealing, most likely due to the lower temperature achieved (*Figure 4 c* and *Figure 6 c*). Comparing dynamic Ebeam and IR, although the dynamic Ebeam treatment could achieve a higher  $PF$  than the dynamic IR after 1 hour of treatment, IR annealing could increase  $PF$  even for 1-min irradiation after the stable temperature was reached, while dynamic Ebeam annealing did not improve  $PF$  until 30 mins of treatment. The shorter treatment time is more desirable for in-line treatment during a R2R process. Therefore, dynamic IR post-deposition treatment seems to be a better approach, to be compatible with a real high-throughput R2R process in an industrial context. Further improvements could be envisaged with a higher power IR source, applied to thinner layers or between successively sputtered layers as might be envisaged for a R2R sputtered process.

The IR heating of the coating on a moving substrate appears to be a promising approach to improve  $PF$  in an in-line process. However, inevitably the IR heating could have some effect on the underlying substrate directly from the radiation or by conduction following absorption by the coating. The tensile mechanical properties and FTIR spectra (*Figure 7*) of the materials (blank PI substrate and Bi-Te films on PI with/without IR anneal) were checked for evidence of any such effect. The tensile modulus of PI film was found to be 1.8 GPa, exactly in the range expected for PI as reported in (69). A blank PI substrate was irradiated under a static IR treatment at 350°C for 1 hour. In *Figure 7 a*, on IR exposure the modulus showed no change in the range of strain: 0 - 1.5% (This is in the elastic region of PI film; once the strain

exceeds such level, the TE property decreased dramatically so our study only considered this strain range). FTIR spectra of PI static-annealed with IR for 1 hour and pristine PI films were compared (*Figure 7 b*). There was no significant difference observed between the spectra. The underlying polymer could however be affected by the much stronger (70) absorption of the IR by the Bi-Te coating from which heat will conduct to the underlying polymer. The Bi-Te coating increased the modulus of both annealed and non-annealed films by about 11% (from 1.8 to 2.0 GPa), however, once again there was no measured effect of the annealing process on the modulus (*Figure 7 c*).

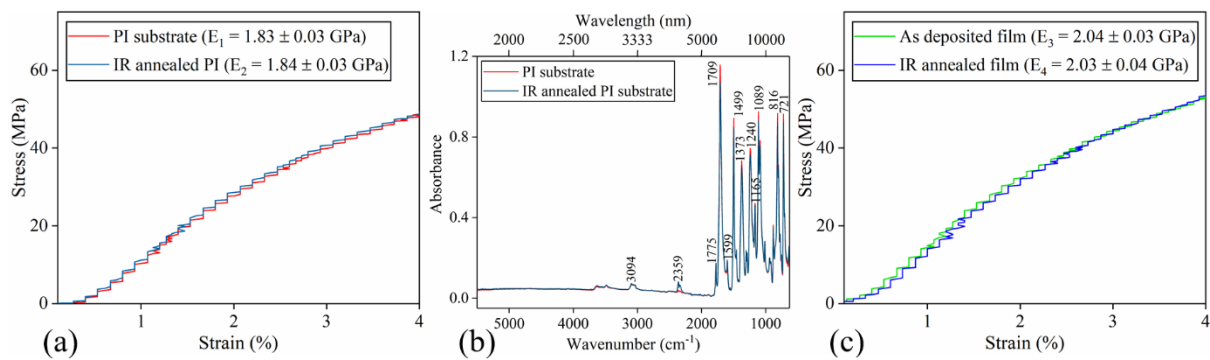


**Figure 7.** (a) Stress-strain relations of polymer substrate and post static IR annealed polymer substrate ( $E$  is the modulus which comes from the strain: 0 - 1.5%); (b) FTIR spectra of polymer substrate and a 1-hour post static IR annealed polymer substrate (the peak at around  $2359 \text{ cm}^{-1}$  comes from  $\text{CO}_2$  in the air); (c) Stress-strain relations of the as-deposited and post dynamic IR annealed films on polymer substrates.

## 4. Conclusion

To investigate feasible post-deposition annealing approaches suitable for R2R processing, we fabricated 1- $\mu\text{m}$  thick Bi-Te films at RT using DC magnetron sputtering onto 125- $\mu\text{m}$  thick PI film, and then post-annealed the coatings using IR and Ebeam irradiation in an industrial-scale R2R webcoater system. In addition, static post-annealing strategies that are commonly



used in the laboratory (i.e. vacuum oven and pulsed Ebeam irradiation) were studied as control groups. The static pulsed Ebeam irradiation was found to be too aggressive showing micro-cracks on the film's surface, confirmed in SEM images, while, as expected/reported, annealing in a vacuum oven significantly improved the film's crystallinity (increasing crystallite size and decreasing micro-strain) and decreased Te content in the film, and *PF* was enhanced by 400%.

Both IR and Ebeam irradiations were compatible with R2R processes. After these two treatments, there was no observed change in the film's crystallinity but the average crystallite size slightly increased. *PF* was improved by 146 % and 64 % after IR and Ebeam irradiations, respectively. The effect of annealing time was further investigated to guide design of a R2R process. After 1-min treatment on a rotating drum, the film annealed with IR irradiation had a much better improvement on *PF* (improved 11.4%) than that annealed in Ebeam irradiation. Hence, IR treatment is more feasible to anneal Bi-Te films in a high throughput R2R process, also because it does not have a significant effect on the mechanical property of PI film.

This study investigated a feasible post-deposition annealing method for flexible TE films to be compatible with high-throughput R2R processes, and achieved an improvement on TE performance by post-deposition annealing Bi-Te films, demonstrating a step forward for commercialisation of flexible TEGs.

## **Corresponding author**

Hazel E. Assender, [hazel.assender@materials.ox.ac.uk](mailto:hazel.assender@materials.ox.ac.uk)

## **Author Contributions**

Xudong Tao: Conceptualization, Methodology, Investigation, Writing – original draft.

Bryan W. Stuart: Investigating, Writing – review & editing.

Kening Wan: Investigating.

James W. Murray: Resources, supervision.

Emiliano Bilotti: Resources, Writing – review & editing.

Hazel E. Assender: Conceptualization, Resources, Writing – review & editing, Supervision.

## **Funding Sources**

Engineering and Physical Sciences Research Council. Grant reference: EP/M015173/1.

K.W.: China Scholarship Council.

## **Acknowledgments**

This study was supported by the Engineering and Physical Sciences Research Council [grant number EP/M015173/1] *via* the Wearable and flexible technologies enabled by advanced thin-film manufacture and metrology (WAFT) K.W. is grateful to the China Scholarship Council for the scholarship support. Collaboration. The authors would like to acknowledge Oxford Materials Characterisation Services (OMSC), Furnace Laboratory Oxford Materials and David Cockayne Centre for Electron Microscopy for equipment access. We would like to especially thank to Dr Colin Johnston, Mrs Jennifer Holter, Dr Clara Barker, Mr Anthony Wheeler and Mr Richard Turner for technical assistance.

## References

- (1) Siddique, A. R. M.; Mahmud, S.; Heyst, B. V. A Review of the State of the Science on Wearable Thermoelectric Power Generators (TEGs) and Their Existing Challenges. *Renew. Sust. Energ. Rev.* **2017**, *73*, 730-744, DOI: 10.1016/j.rser.2017.01.177.
- (2) Glatzmaier, G. C.; Rea, J.; Olsen, M. L.; Oshman, C.; Hardin, C.; Alleman, J.; Sharp, J.; Weigand, R.; Campo, D.; Hoeschele, G.; Parilla, P. A.; Siegel, N. P.; Toberer, E. S.; Ginley, D. S. Solar Thermoelectricity via Advanced Latent Heat Storage: A Cost-effective Small-scale CSP Application. *AIP Conf Proc.* **2017**, *1850*, 300191, DOI: 10.1063/1.4984362.
- (3) Bailini, A.; Donati, F.; Zamboni, M.; Russo, V.; Passoni, M.; Casari, C. S.; Li Bassi, A.; Bottani, C. E. Pulsed Laser Deposition of Bi<sub>2</sub>Te<sub>3</sub> Thermoelectric Films. *Appl. Surf. Sci.* **2007**, *254*, 1249-1254, DOI: //doi.org/10.1016/j.apsusc.2007.09.039.
- (4) Cho, S.; Kim, Y.; DiVenere, A.; Wong, G. K.; Ketterson, J. B.; Meyer, J. R. Antisite Defects of Bi<sub>2</sub>Te<sub>3</sub> Thin Films. *Appl. Phys. Lett.* **1999**, *75*, 1401-1403, DOI: 10.1063/1.124707.
- (5) Giani, A.; Pascal-Delannoy, F.; Boyer, A.; Foucaran, A.; Gschwind, M.; Ancey, P. Elaboration of Bi<sub>2</sub>Te<sub>3</sub> by Metal Organic Chemical Vapor Deposition. *Thin Solid Films* **1997**, *303*, 1-3, DOI: //doi.org/10.1016/S0040-6090(97)00089-8.
- (6) Boulouze, A.; Boulouze, M.; Giani, A.; Pascal-Delannoy, F.; Foucaran, A.; Boyer, A. Preparation and Characterization of MOCVD Bismuth Telluride Thin Films. *J. Cryst. Growth* **1998**, *194*, 336-341, DOI: 10.1016/S0022-0248(98)00690-3.
- (7) Miyazaki, Y.; Kajitani, T. Preparation of Bi<sub>2</sub>Te<sub>3</sub> Films by Electrodeposition. *J. Cryst. Growth* **2001**, *229*, 542-546, DOI: 10.1016/S0022-0248(01)01225-8.
- (8) Dheepa, J.; Sathyamoorthy, R.; Subbarayan, A. Optical Properties of Thermally Evaporated Bi<sub>2</sub>Te<sub>3</sub> Thin Films. *J. Cryst. Growth* **2005**, *274*, 100-105, DOI: 10.1016/j.jcrysgro.2004.09.070.
- (9) Zou, H.; Rowe, D. M.; Min, G. Growth of p- and n-type Bismuth Telluride Thin Films by Co-evaporation. *J. Cryst. Growth* **2001**, *222*, 82-87, DOI: 10.1016/S0022-0248(00)00922-2.
- (10) Murmu, P. P.; Kennedy, J.; Suman, S.; Chong, S. V.; Leveneur, J.; Storey, J.; Rubanov, S.; Ramanath, G. Multifold Improvement of Thermoelectric Power Factor by Tuning Bismuth and Antimony in Nanostructured n-type Bismuth Antimony Telluride Thin Films. *Mater. Des.* **2019**, *163*, 1075491-1075497, DOI: 10.1016/j.matdes.2018.107549.
- (11) Kim, D.; Byon, E.; Lee, G.; Cho, S. Effect of Deposition Temperature on the Structural and Thermoelectric Properties of Bismuth Telluride Thin Films Grown by Co-sputtering. *Thin Solid Films* **2006**, *510*, 148-153, DOI: 10.1016/j.tsf.2005.12.306.

- (12) Huang, H.; Luan, W.; Tu, S. Influence of Annealing on Thermoelectric Properties of Bismuth Telluride Films Grown via Radio Frequency Magnetron Sputtering. *Thin Solid Films* **2009**, *517*, 3731-3734, DOI: 10.1016/j.tsf.2009.01.015.
- (13) Madou, M. J. Manufacturing Techniques for Microfabrication and Nanotechnology. *CRC Press*. **2011**, 403-404, DOI: 10.1201/9781439895306.
- (14) Taylor; Cliffordl; Bjornard; Erikj; Valiska; Michaelj. Film Thickness Uniformity Control Apparatus for In-line Sputtering Systems. *US patents* **1992**, 1-7.
- (15) Wei, Z.; Bobbili, P. R.; Senthilarasu, S.; Shimell, T.; Upadhyaya, H. M. Design and Optimisation of Process Parameters in an In-line CIGS Evaporation Pilot System. *Surf. Coat. Technol.* **2014**, *241*, 159-167, DOI: 10.1016/j.surfcoat.2013.10.033.
- (16) Shen, J.; Zhu, T.; Zhao, X.; Zhang, S.; Yang, S.; Yin, Z. Recrystallization Induced in situ Nanostructures in Bulk Bismuth Antimony Tellurides: A Simple Top Down Route and Improved Thermoelectric Properties. *Energy Environ. Sci.* **2010**, *3*, 1519-1523, DOI: 10.1039/C0EE00012D.
- (17) Manzano, C. V.; Abad, B.; Rojo, M. M.; Koh, Y. R.; Hodson, S. L.; Martinez, A. M. L.; Xu, X.; Shakouri, A.; Sands, T. D.; Borca-Tasciuc, T. Anisotropic Effects on the Thermoelectric Properties of Highly Oriented Electrodeposited Bi<sub>2</sub>Te<sub>3</sub> Films. *Sci. Rep.* **2016**, *6*, 19129, DOI: 10.1038/srep19129.
- (18) Fleurial, J. P.; Gailliard, L.; Triboulet, R.; Scherrer, H.; Scherrer, S. Thermal Properties of High Quality Single Crystals of Bismuth Telluride—Part I: Experimental Characterization. *J Phys Chem Solids* **1988**, *49*, 1237-1247, DOI: 10.1016/0022-3697(88)90182-5.
- (19) Goldsmid, H. J. Thermoelectric Refrigeration. *Springer* **1964**, 133-161.
- (20) Duan, X.; Jiang, Y. Annealing Effects on the Structural and Electrical Transport Properties of n-type Bi<sub>2</sub>Te<sub>2.7</sub>Se<sub>0.3</sub> Thin Films Deposited by Flash Evaporation. *Appl. Surf. Sci.* **2010**, *256*, 7365-7370, DOI: 10.1016/j.apsusc.2010.05.069.
- (21) Zheng, Z.; Fan, P.; Liang, G.; Zhang, D.; Cai, X.; Chen, T. Annealing Temperature Influence on Electrical Properties of Ion Beam Sputtered Bi<sub>2</sub>Te<sub>3</sub> Thin Films. *J Phys Chem Solids* **2010**, *71*, 1713-1716, DOI: 10.1016/j.jpcs.2010.09.012.
- (22) Hashibon, A.; Elsässer, C. First-principles Density Functional Theory Study of Native Point Defects in Bi<sub>2</sub>Te<sub>3</sub>. *Phys. Rev. B* **2011**, *84*, 1441171-1441179, DOI: 10.1103/PhysRevB.84.144117.
- (23) Kim, J.; Choi, J.; Bae, J.; Kim, M.; Oh, T. Thermoelectric Characteristics of n-Type Bi<sub>2</sub>Te<sub>3</sub> and p-Type Sb<sub>2</sub>Te<sub>3</sub> Thin Films Prepared by Co-Evaporation and Annealing for Thermopile Sensor Applications. *Mater. Trans.* **2013**, *54*, 618-625, DOI: 10.2320/matertrans.M2013010.

- (24) Na, J.; Kim, Y.; Park, T.; Park, C.; Kim, E. Preparation of Bismuth Telluride Films with High Thermoelectric Power Factor. *ACS Appl. Mater. Interfaces* **2016**, *8*, 32392-32400, DOI: 10.1021/acsami.6b10188.
- (25) Kim, Y.; Cho, S.; DiVenere, A.; Wong, G. K. L.; Ketterson, J. B. Composition-dependent Layered Structure and Transport Properties in BiTe Thin Films. *Phys. Rev. B* **2001**, *63*, 1553061-1553065, DOI: 10.1103/PhysRevB.63.155306.
- (26) N. Peranio; O. Eibl. Structural and Thermoelectric Properties of Epitaxially Grown Bi<sub>2</sub>Te<sub>3</sub> Thin Films and Superlattices. *J. Appl. Phys.* **2006**, *100*, 1143061-11430610, DOI: 10.1063/1.2375016.
- (27) Sudarshan, C.; Jayakumar, S.; Vaideki, K.; Sudakar, C. Effect of Vacuum Annealing on Structural, Electrical and Thermal Properties of E-beam Evaporated Bi<sub>2</sub>Te<sub>3</sub> Thin Films. *Thin Solid Films* **2017**, *629*, 28-38, DOI: 10.1016/j.tsf.2017.03.043.
- (28) Singkaselit, K.; Sakulkalavek, A.; Sakdanuphab, R. Effects of Annealing Temperature on the Structural, Mechanical and Electrical Properties of Flexible Bismuth Telluride Thin Films Prepared by High-pressure RF Magnetron Sputtering. *ANSN* **2017**, *8*, 350021-350027, DOI: 10.1088/2043-6254/aa7222.
- (29) Takemori, D.; Okuhata, M.; Takashiri, M. Thermoelectric Properties of Electrodeposited Bismuth Telluride Thin Films by Thermal Annealing and Homogeneous Electron Beam Irradiation. *ECS Trans* **2017**, *75*, 123-131, DOI: 10.1149/07552.0123ecst.
- (30) Kudo, S.; Tanaka, S.; Miyazaki, K.; Nishi, Y.; Takashiri, M. Anisotropic Analysis of Nanocrystalline Bismuth Telluride Thin Films Treated by Homogeneous Electron Beam Irradiation. *Mater. Trans.* **2017**, *58*, 513-519, DOI: 10.2320/matertrans.M2016295.
- (31) Takashiri, M.; Uyama, M.; Imai, K. Comparison of Crystal Growth and Thermoelectric Properties of n-type Bi-Se-Te and p-type Bi-Sb-Te Nanocrystalline Thin Films: Effects of Homogeneous Irradiation with an Electron Beam. *J. Appl. Phys.* **2014**, *115*, 2143111-2143117, DOI: 10.1063/1.4881676.
- (32) Chatterjee, K.; Suresh, A.; Ganguly, S.; Kargupta, K.; Banerjee, D. Synthesis and Characterization of an Electro-deposited Polyaniline-Bismuth Telluride Nanocomposite — A Novel Thermoelectric Material. *Mater. Charact.* **2009**, *60*, 1597-1601, DOI: 10.1016/j.matchar.2009.09.012.
- (33) Carroll, E.; Buckley, D.; Mogili, N. V. V.; McNulty, D.; Moreno, M. S.; Glynn, C.; Collins, G.; Holmes, J. D.; Razeed, K. M.; O'Dwyer, C. 2D Nanosheet Paint from Solvent-Exfoliated Bi<sub>2</sub>Te<sub>3</sub> Ink. *Chem. Mater.* **2017**, *29*, 7390-7400, DOI: 10.1021/acs.chemmater.7b02321.
- (34) Mohammed Khalaf, E. Improvement of Chemical and Thermal Properties of Polyethylene Terephthalate (PET) by Using Multi-walled Carbon Nanotubes (MWCNTs). *IJMSA* **2016**, *5*, 297-301, DOI: 10.11648/j.ijmsa.20160506.20.

- (35) Maurer, M. L.; Tooker, A. C.; Felix, S. H. Characterization of Polyimide via FTIR Analysis. *SciTech Connect.* **2014**, 1-8.
- (36) Ozur, G. E.; Proskurovsky, D. I. Generation of Low-Energy High-Current Electron Beams in Plasma-Anode Electron Guns. *Plasma Phys. Rep* **2018**, *44*, 18-39, DOI: 10.1134/s1063780x18010130.
- (37) Greenaway, D. L.; Harbeke, G. Band Structure of Bismuth Telluride, Bismuth Selenide and Their Respective Alloys. *J Phys Chem Solids* **1965**, *26*, 1585-1604, DOI: 10.1016/0022-3697(65)90092-2.
- (38) Kaddouri, E. H.; Maurice, T.; Gratens, X.; Charar, S.; Benet, S.; Mefleh, A.; Tedenac, J. C.; Liautard, B. Optical Properties of Bismuth Telluride Thin Films, Bi<sub>2</sub>Te<sub>3</sub>/Si(100) and Bi<sub>2</sub>Te<sub>3</sub>/SiO<sub>2</sub>/Si(100). *Phys. Status Solidi* **1999**, *176*, 1071-1076, DOI: 10.1002/(SICI)1521-396X(199912)176:23.0.CO;2-E.
- (39) Williamson, G. K.; Hall, W. H. X-ray Line Broadening from Filled Aluminium and Wolfram. *Acta Metall.* **1953**, *1*, 22-31, DOI: 10.1016/0001-6160(53)90006-6.
- (40) Langford, J. I.; Wilson, A. J. C. Scherrer after Sixty Years: A Survey and Some New Results in the Determination of Crystallite Size. *J. Appl. Crystallogr.* **1978**, *11*, 102-113, DOI: 10.1107/S0021889878012844.
- (41) Deng, Y.; Liang, H.; Wang, Y.; Zhang, Z.; Tan, M.; Cui, J. Growth and Transport Properties of Oriented Bismuth Telluride Films. *J. Alloys Compd.* **2011**, *509*, 5683-5687, DOI: 10.1016/j.jallcom.2011.02.123.
- (42) Zhang, J. X.; Li, Q.; Niu, P. J.; Yang, Q. X.; Tan, B. M.; Niu, X. H.; Gao, B. H. Effect of Annealing Temperature on Microstructure and Thermoelectric Properties of Bismuth-Telluride Multilayer Thin Films Prepared by Magnetron Sputtering. *Mater. Res. Innov.* **2015**, *19*, S10-412, DOI: 10.1179/1432891715Z.0000000002209.
- (43) Vieira, E.; Figueira, J.; Pires, A. L.; Grilo, J.; Silva, M. F.; Pereira, A. M.; Goncalves, L. M. Bi<sub>2</sub>Te<sub>3</sub> and Sb<sub>2</sub>Te<sub>3</sub> Thin Films with Enhanced Thermoelectric Properties for Flexible Thermal Sensors. *Proceedings* **2018**, *2*, 8151-8154, DOI: 10.3390/proceedings2130815.
- (44) El-Sayed, H. E. A. Structural and Optical Properties of Thermally Evaporated Bi<sub>2</sub>Te<sub>3</sub> Films. *Appl. Surf. Sci.* **2005**, *250*, 70-78, DOI: 10.1016/j.apsusc.2004.12.025.
- (45) G. D. Deshmukh; S. M. Patil; S. S. Patil; P. H. Pawar. Effect of Film Thickness on Structural and Optical Properties of Bi<sub>2</sub>Te<sub>3</sub> Thin Films. *J. chem. biol. phys. sci.* **2015**, *5*, 2769-2779.
- (46) Liao, C.; Liou, K. Electric Current Enhanced Defect Elimination in Thermally Annealed Bi-Sb-Te and Bi-Se-Te Thermoelectric Thin Films. *J. Appl. Phys.* **2010**, *108*, 537111, DOI: 10.1063/1.3477184.

- (47) Faraji, L. S.; Singh, R. P.; Allahkarami, M. Pulsed Laser Deposition of Bismuth Telluride Thin Film and Annealing Effects. *EPJ Appl. Phys.* **2009**, *46*, 205011-205015, DOI: 10.1051/epjap/2009053.
- (48) Kim, H.; Yim, J.; Choi, W.; Park, C.; Kim, J. The Effect of Annealing in Controlled Vapor Pressure on the Thermoelectric Properties of RF-Sputtered Bi<sub>2</sub>Te<sub>3</sub> Film. *Journal of Elec Materi* **2012**, *41*, 1519-1523, DOI: 10.1007/s11664-012-1938-4.
- (49) Navone, C.; Soulier, M.; Plissonnier, M.; Seiler, A. L. Development of (Bi,Sb)<sub>2</sub>(Te,Se)<sub>3</sub>-Based Thermoelectric Modules by a Screen-Printing Process. *J. Electron. Mater.* **2010**, *39*, 1755–1759, DOI: 10.1007/s11664-010-1187-3.
- (50) Miyazaki, K.; Kurosaki, J.; Takashiri, M.; Tsukamoto, H.; Tanaka, S.; Nagai, D. Effect of Grain Size on Thermoelectric Properties of n-type Nanocrystalline Bismuth-Telluride Based Thin Films. *J. Appl. Phys.* **2008**, *104*, 843021, DOI: 10.1063/1.2990774.
- (51) Krumrain, J.; Mussler, G.; Borisova, S.; Stoica, T.; Plucinski, L.; Schneider, C. M.; Grtzmacher, D. MBE Growth Optimization of Topological Insulator Bi<sub>2</sub>Te<sub>3</sub> Films. *J. Cryst. Growth* **2011**, *324*, 115-118, DOI: 10.1016/j.jcrysgro.2011.03.008.
- (52) Pilaipon Nuthongkum; Rachsak Sakdanuphab; Mati Horprathum; Aparporn Sakulkalavek [Bi]:[Te] Control, Structural and Thermoelectric Properties of Flexible Bi<sub>2</sub>Te<sub>3</sub> Thin Films Prepared by RF Magnetron Sputtering at Different Sputtering Pressures. *J. Electron. Mater.* **2017**, *46*, 6444–6450, DOI: 10.1007/s11664-017-5671-x.
- (53) Lanson, B. Decomposition of Experimental X-ray Diffraction Patterns (Profile Fitting): A Convenient Way to Study Clay Minerals. *Clays Clay Miner.* **1997**, *45*, 132-146, DOI: 10.1346/CCMN.1997.0450202.
- (54) Arunachalam, A.; Dhanapandian, S.; Manoharan, C.; Sivakumar, G. Physical Properties of Zn Doped TiO<sub>2</sub> Thin Films with Spray Pyrolysis Technique and its Effects in Antibacterial Activity. *Spectrochim. Acta A Mol. Biomol. Spectrosc.* **2015**, *138*, 105-112, DOI: 10.1016/j.saa.2014.11.016.
- (55) Park, N.; Lee, W.; Hong, J.; Park, T.; Yoon, S.; Im, H.; Kim, H.; Lee, S. Effect of Grain Size on Thermal Transport in Post-annealed Antimony Telluride Thin Films. *Nanoscale Res Lett* **2015**, *10*, 1-9, DOI: 10.1186/s11671-015-0733-6.
- (56) Chu, H.; Liou, K.; Liao, C. Enhancement of Thermoelectric Properties of Sputtered Bi-Sb-Te Thin Films by Electric Current Stressing. *Appl. Phys. Lett.* **2008**, *93*, 421031, DOI: 10.1063/1.2965487.
- (57) Snyder, G. J.; Toberer, E. S. Complex Thermoelectric Materials. *Nat. Mater.* **2008**, *7*, 105-114, DOI: 10.1038/nmat2090.
- (58) Levin, E. M. Charge Carrier Effective Mass and Concentration Derived from Combination of Seebeck coefficient and Te<sup>125</sup> NMR Measurements in Complex Tellurides. *Phys. Rev. B* **2016**, *93*, 2452021-2452025, DOI: 10.1103/PhysRevB.93.245202.

- (59) Petsagkourakis, I.; Pavlopoulou, E.; Cloutet, E.; Chen, Y. F.; Liu, X.; Fahlman, M.; Berggren, M.; Crispin, X.; Dilhaire, S.; Fleury, G.; Hadziioannou, G. Correlating the Seebeck coefficient of Thermoelectric Polymer Thin Films to their Charge Transport Mechanism. *Org. Electron.* **2018**, *52*, 335-341, DOI: 10.1016/j.orgel.2017.11.018.
- (60) Damodara Das, V.; Soundararajan, N.; Pattabi, M. Electrical Conductivity and Thermoelectric Power of Amorphous Sb<sub>2</sub>Te<sub>3</sub> Thin Films and Amorphous-crystalline Transition. *J. Mater. Sci.* **1987**, *22*, 3522-3528, DOI: 10.1007/BF01161452.
- (61) H Julian Goldsmid Bismuth Telluride and Its Alloys as Materials for Thermoelectric Generation. *Materials* **2014**, *7*, 2577-2592, DOI: 10.3390/ma7042577.
- (62) K Sharma; M Lal; V K Gumber; A Kumar; N Chaudary; N Goyal. Effect of Composition on Optical and Thermoelectric Properties of Microstructured p-type (Bi<sub>2</sub>Te<sub>3</sub>)<sub>x</sub>(Sb<sub>2</sub>Te<sub>3</sub>)<sub>1-x</sub> Alloys. *J. Nano- Electron. Phys.* **2014**, *6*, 1007-1, DOI: 2077-6772/2014/6(1)01007(6).
- (63) Gibbs, Z. M.; Kim, H.; Wang, H.; Snyder, G. J. Band Gap Estimation from Temperature Dependent Seebeck Measurement—Deviations from the  $2e|S|_{\max}T_{\max}$  Relation. *Appl. Phys. Lett.* **2015**, *106*, 221121-221125, DOI: 10.1063/1.4905922.
- (64) M. Bachmann, M. Czerner, and C. Heiliger. Ineffectiveness of Energy Filtering at Grain Boundaries for Thermoelectric Materials. *Phys. Rev. B*, *86*, 1153201- 1153206, DOI: 10.1103/PhysRevB.86.115320.
- (65) Hada, M.; Norimatsu, K.; Tanaka, S.; Keskin, S.; Tsuruta, T.; Igarashi, K.; Ishikawa, T.; Kayanuma, Y.; Miller, R. J. D.; Onda, K.; Sasagawa, T.; Koshihara, S.; Nakamura, K. G. Bandgap Modulation in Photoexcited Topological Insulator Bi<sub>2</sub>Te<sub>3</sub> via Atomic Displacements. *J. Chem. Phys.* **2016**, *145*, 245041, DOI: 10.1063/1.4955188.
- (66) Tao, X.; Wan, K.; Deru, J.; Bilotti, E.; Assender, H. E. Thermoelectric Behaviour of Bi-Te Films on Polymer Substrates DC-sputtered at Room-temperature in Moving Web Deposition. *Surf. Coat. Technol.* **2020**, *385*, 1253931-1253939, DOI: 10.1016/j.surfcoat.2020.125393.
- (67) Lal, S.; Gautam, D.; Razeeb, K. M. Optimization of Annealing Conditions to Enhance Thermoelectric Performance of Electrodeposited p-type BiSbTe Thin Films. *APL Mater.* **2019**, *7*, 311021, DOI: 10.1063/1.5049586.
- (68) Lu, J.; Guo, R.; Dai, W.; Huang, B. Enhanced Thermoelectric Figure-of-Merit in Boron-doped SiGe Thin Films by Nanograin Boundaries. *Nanoscale* **2014**, *7*, 7331-7339, DOI: 10.1039/c5nr00181a.
- (69) Yao, J.; Wang, C.; Tian, C.; Zhao, X.; Zhou, H.; Wang, D.; Chen, C. Highly Optical Transparency and Thermally Stable Polyimides Containing Pyridine and Phenyl Pendant. *Des Monomers Polym.* **2017**, *20*, 449-457, DOI: 10.1080/15685551.2017.1351766.
- (70) Stuart, B. W.; Tao, X.; Gregory, D.; Assender, H. E. Roll-to-Roll Patterning of Al/Cu/Ag Electrodes on Flexible Polyethylene by Oil Masking: A comparison of Thermal



Evaporation and Magnetron Sputtering. *Appl. Surf. Sci.* **2019**, 1442941-14429413, DOI: 10.1016/j.apsusc.2019.144294.